



Application of neutron imaging to detect and quantify fatigue cracking

A Reid^{a,*}, M Marshall^a, S Kabra^b, T Minniti^b, W Kockelmann^b, T Connolley^c, A James^d, TJ Marrow^e, M Mostafavi^d

^a University of Sheffield, Department of Mechanical Engineering, Sheffield S1 3JD, United Kingdom

^b STFC-Rutherford Appleton Laboratory, ISIS Facility, Harwell OX11 0QX, United Kingdom

^c Diamond Light Source Ltd., Harwell Science and Innovation Campus, Didcot, Oxfordshire OX11 0DE, United Kingdom

^d University of Bristol, Department of Mechanical Engineering, Bristol BS8 1TR, United Kingdom

^e University of Oxford, Department of Materials, Oxford, OX1 3BD, United Kingdom

ARTICLE INFO

Keywords:

Duplex stainless steel
Energy-dispersive imaging
Bragg edge transmission imaging
Neutron computed tomography
X-ray computed tomography

ABSTRACT

Non-destructive imaging techniques provide a unique opportunity to study crack initiation and propagation behaviour in structural materials. To evaluate the applicability of different volumetric imaging techniques, a round bar notched sample of duplex stainless steel was fatigue cracked and studied in situ and ex situ. Neutron and synchrotron X-ray tomography was used along with destructive methods and Bragg edge neutron imaging to evaluate the fatigue crack. Neutron attenuation tomography obtained a three-dimensional image in which the crack was readily identifiable. The neutron tomography, although lower in spatial resolution compared with the X-ray synchrotron tomography and requiring higher acquisition time, is sensitive to the phase chemistry, and has the potential to study engineering size components. Bragg edge neutron transmission imaging allows for the mapping of two-dimensional elastic strains and was used to identify the fatigue crack from the reduction in the strain in the region where the crack propagated. A finite element model of the cracked specimen was used to simulate the average through thickness strain that is measured by the Bragg edge neutron imaging technique. The strains measured in the ferritic phase correspond better with the simulation strains than the strain measured in the austenitic phase. It is concluded that this difference is due to strain partitioning, which is influenced by the strong texture present in the duplex steel.

1. Introduction

Structural integrity assessments are important tools when aiming to safely predict the longevity of service components. Many such assessments consider the most common damage mechanisms of engineering components, offering models for fatigue life predictions. Developing a comprehensive understanding of fatigue crack initiation and propagation to inform the models is therefore of great engineering importance. Such predictive models can be used to forecast the fatigue life of service components, with the aim of reducing cost while maintaining safety. Validating fatigue life estimations through comparison with experimental results of non-destructive and destructive techniques is pivotal [1–3]. However, fatigue failure is microstructurally sensitive [4], and is best described by probabilistic processes. Models for predicting fatigue life are inherently statistical, making their validation difficult. Detecting fatigue cracks is particularly challenging and has been the subject of research for many years.

Destructive micromechanical methods (e.g. serial sectioning [5]) to detect crack initiation sites and propagation paths are well-established.

Non-destructive techniques, for example acoustic emission (AE) combined with advanced signal processing [6], offer in situ analysis of propagating cracks, though with lower resolution than destructive methods. Optical techniques to identify crack initiation, as well as quantifying associated parameters, such as opening displacement, are widely used in academic studies. One such technique, that is gaining popularity in recent years, is optical or scanning electron microscopy combined with digital image correlation [7]. Digital image correlation (DIC) is now a routine full-field technique for surface displacement measurements and has previously been used, in conjunction with finite element analysis, to calculate crack driving forces [8]. DIC tracks the displacement of a surface speckle pattern before and after material deformation, which makes the calculation of full-field displacement possible. Similar to digital image correlation analysis of surface cracks, digital volume correlation (DVC), applied on laboratory or synchrotron X-ray tomography, has been demonstrated to quantify cracks within the material [9,10]. While DIC analysis of surface cracks is applicable to all materials, the DVC analysis is only possible on materials which have the appropriate speckle pattern required for image correlation inside them. This prerequisite limits

* Corresponding author.

E-mail address: agpreid1@sheffield.ac.uk (A. Reid).

<https://doi.org/10.1016/j.ijmecsci.2019.05.037>

Received 21 December 2018; Received in revised form 30 April 2019; Accepted 26 May 2019

Available online 27 May 2019

0020-7403/© 2019 The Authors. Published by Elsevier Ltd. This is an open access article under the CC BY license. (<http://creativecommons.org/licenses/by/4.0/>)

DVC analysis to materials that are composite (e.g. Aluminium Titanium metal matrix composites [11] or nodular cast iron [12]) or heterogeneous materials (e.g. nuclear graphite [13] or wood [14]).

Computed tomographic imaging, performed for DVC, is also useful to study the behaviour of fatigue cracks because of the three-dimensional nature of the crack propagation path [15]. The two widely used techniques are X-ray (laboratory and synchrotron) and neutron tomography. Advances in X-ray imaging are well reported [16–18], notably as it is developed in parallel with medical research [19]. Neutron imaging techniques, however, have been less advanced due to the limited number of instruments capable of offering the technique. Both X-ray and neutron tomography have their advantages and disadvantages, for example neutrons can penetrate greater depths in most metallic systems, such as steel, when compared to X-rays, making them more suited for studying engineering components [20]. However, the lower spatial resolution of neutron tomography and often longer acquisition times mean that detailed analysis of smaller features [21], such as cracks, is difficult. The two techniques (X-ray and neutron tomography) provide complementary information, potentially adding more value when used in conjunction with one another for more in-depth analysis. Presently, the UK's dedicated neutron imaging beamline, IMAT, at ISIS Muon and Neutron Source, is advancing time-of-flight (ToF) neutron imaging, energy dispersive radiography, and white-beam tomography for engineering [22] and material science [23] applications.

Duplex Stainless Steels are important for corrosion resistant applications [24]. Duplex stainless steels have two microstructural phases, usually with near equal phase volumes, of ferrite and austenite steel [25]. This complex microstructure, which is often accompanied by internal residual stresses and strong textures, makes predicting the fatigue behaviours of duplex steels complicated [26]. For very high cycle fatigue, it has been suggested that crack nucleation sites generally occur at the phase boundaries on the materials surface [27], yet the presence of non-metallic inclusions has been found to initiate cracking in the material subsurface [28]. Also, much work has focused on low cycle fatigue [25,26], whilst medium cycle fatigue regime for duplex steel is less understood [31].

The aim of this study is to investigate medium cycle fatigue crack nucleation and propagation in a duplex stainless steel, Alloy 2205, using two neutron imaging techniques: Bragg edge transmission imaging and neutron computed tomography (NCT). While neutron Bragg edge imaging allows measurement of the average elastic strain variation through the thickness of a sample, neutron computed tomography visualises the three-dimensional internal structure. Bragg edge transmission imaging has successfully been used to examine the residual strain developed during additive manufacturing of Inconel 625, via direct metal laser melting [32]. A recent study measured the compressive residual strain beneath the surface of a laser-shock peened plate [33]. The technique has also been employed to map the strain field around a fatigue crack propagating through X70 steel [34]. The neutron imaging techniques were complemented by parallel beam, synchrotron X-ray computed tomography (XCT) and the results of these various non-destructive techniques were validated using destructive, post-mortem scanning electron microscopy. The literature on crack detection using XCT is rich [35] but there are few studies that report crack detection and quantification using Bragg edge transmission imaging or NCT [36,37]. This is partly due to the novelty of detectors and instruments that are capable of making such techniques more widely available. Future approaches could potentially combine three-dimensional Bragg edge transmission imaging with neutron tomography and DVC to study the elastic and plastic behaviour of materials.

This paper will assess the extent and limitation of neutron imaging techniques to identify and quantify crack nucleation and propagation. In addition, both neutron techniques will be shown to be able to distinguish different phases of the duplex steel as well as quantifying strain partitioning between the phases. In particular, NCT, unlike XCT, allows for different phases in the material to be identified.

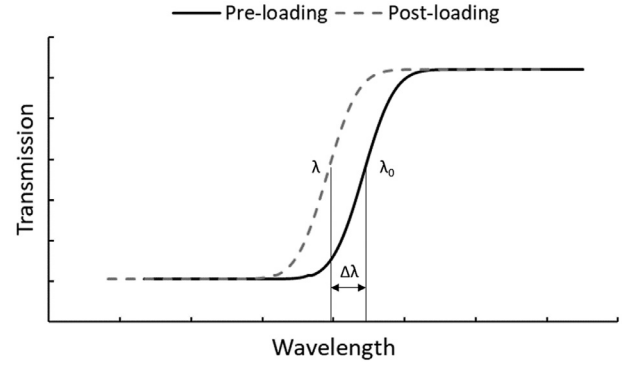


Fig. 1. A Bragg edge pre-loading and post-loading, with an exaggerated shift to demonstrate the effect used to calculate elastic strain.

2. Background

2.1. Bragg edge transmission imaging

In Bragg edge neutron transmission imaging, the incident neutron beam is directed at the sample and a neutron counting detector is placed directly behind the sample. The arrangement allows for measurement of Time of Flight (ToF) for individual transmitted neutrons through the sample. The ToF measurements of individual neutrons are used to calculate their wavelength:

$$\lambda = \frac{ht}{mL} \quad (1)$$

where λ is the wavelength of the neutron, t its time of flight, h is Planck's constant (6.626×10^{-34} Js), m is the mass of the neutron (1.675×10^{-27} kg), and L is the path length of the neutron (beamline specific). A spectrum comprising the intensity of neutrons passed through the sample as a function of their wavelength can therefore be created. Transmission spectra contain distinctive increases of intensity, associated with the neutron wavelength at which Bragg's law ($2d\sin(\theta) = n\lambda$, where θ is the angle between the neutron beam and the lattice plane, d is the lattice spacing and n is an integer) is no longer satisfied for a given family of (hkl) lattice planes [34]. At this neutron wavelength, 2θ angle becomes greater than 180° for the given (hkl) and neutrons of energies lower (higher wavelength) than this are transmitted and no longer diffracted. An increase of intensity is observed at this wavelength in the transmission spectrum, known as a Bragg edge [38,39]. A Bragg edge wavelength corresponds to twice the interplanar lattice spacing and is analogous to a Bragg peak, in that shifts in the Bragg edge position can be used to calculate elastic strain:

$$\epsilon = \frac{d - d_0}{d_0} = \frac{\lambda - \lambda_0}{\lambda_0} = \frac{\Delta\lambda}{\lambda_0} \quad (2)$$

where, d is the lattice spacing, d_0 is the stress free lattice spacing, λ is the wavelength at Bragg edge position and λ_0 is the stress-free Bragg edge position; $\Delta\lambda$ is shown in Fig. 1 schematically which demonstrates an exaggerated Bragg edge shift, caused by the application of a compressive load.

It has been shown that an analytical function can be used to fit a Bragg edge, giving a wavelength position in the transmission spectrum [32]:

$$T(\lambda) = C_1 + C_2 \left[\operatorname{erfc} \left(\frac{\lambda_{hkl} - \lambda}{\sqrt{2}\sigma} \right) - \exp \left(\frac{\lambda_{hkl} - \lambda}{\tau} + \frac{\sigma^2}{2\tau^2} \right) \operatorname{erfc} \left(\frac{\lambda_{hkl} - \lambda}{\sqrt{2}\sigma} + \frac{\sigma}{\sqrt{2}\tau} \right) \right] \quad (3)$$

where $T(\lambda)$ is transmission intensity at wavelength λ , λ_{hkl} is the wavelength of the Bragg edge associated with (hkl) plane, σ is the edge width,

τ is the edge asymmetry, and C_1 and C_2 are constants related to the offset and height of the edge, respectively. The function was used to plot the Bragg edges in Fig. 1. Bragg edge imaging has been successfully used to measure through thickness average elastic strain with $\Delta \approx 10^{-5}$ accuracy [40].

The Bragg edge transmission imaging technique generates two-dimensional maps of elastic strain over the entire detector field of view (FoV) in a single scan. The strain map will have a spatial resolution dependent on the detector's pixel size [41]. Producing a strain map with similar spatial resolution using conventional powder diffraction method requires many point measurements with a total acquisition time dependent on the number of points being collected and the chosen gauge volume, which often exceeds the acquisition time of single shot Bragg edge transmission imaging by orders of magnitude [13]. However, it should be noted that in a conventional powder diffraction measurement the combined use of slits and collimators on the incident and diffracted beam allows for a cuboid gauge volume to be defined within the sample. Conversely, a Bragg edge scan measures the elastic strain component parallel to the incident beam direction, averaged through the sample thickness. This may be beneficial or disadvantageous depending on the sample geometry and desired strain component to be measured.

2.2. Computed tomography

An alternative three-dimensional technique is attenuation-based computed tomography (CT) in which a volumetric image of the features based on their attenuation coefficient is created. The volumetric image allows for non-destructive interrogation of the features within the sample, including cracks [42]. Methodologically, neutron and X-ray CT are similar, although they are based on different physics laws: whilst X-rays interact with the atoms valence electrons, thermal neutrons interact with the nuclei of the atom [43]. In both techniques, projections of transmitted X-rays or neutrons at multiple angles are captured by an appropriate detector. The projections are then reconstructed into a 3D image using a reconstruction algorithm, depending on the type of CT performed and the data quality [44]. For the attenuation of X-rays and thermal neutrons the Beer-Lambert law is valid [45]. Eq. (4) demonstrates the simplified Beer-Lambert law of exponential attenuation for monoenergetic incident radiation to allow for a direct comparison of the principles of neutron and X-ray CT.

$$I = I_0 e^{(-Bx)} \quad (4)$$

In this equation I is the transmitted intensity, I_0 is the initial intensity, B is an attenuation coefficient, and x is distance transmitted through the substance.

For X-rays, B is the linear attenuation coefficient, which can be calculated using the product of the mass attenuation coefficient and the material density. This coefficient, for a given energy, will increase for atoms with a greater number of electrons, or higher atomic number [46]. For neutrons, B is often referred to as the total macroscopic cross-section, Σ , and represents the effective interactive area of all nuclei within a certain volume [20]. Values of Σ for a given neutron energy are calculated from the material density, atomic weight and the microscopic cross-section, depending on the type of interaction that has occurred, e.g. absorption or scattering. Eq. (5) calculates the macroscopic cross-section:

$$\Sigma = \frac{\rho}{A} N_A (\sigma_a + \sigma_s) = \frac{\rho}{A} N_A \sigma_t \quad (5)$$

where Σ is the macroscopic cross-section, A is material cross-sectional area, N_A is Avogadro's constant, σ_a is the absorption microscopic cross-section, σ_s is the scattering microscopic cross-section, σ_t is the total microscopic cross-section and ρ is the material density.

Synchrotron X-ray micro-CT has become a well-established method for inspecting material damage including cracks, voids and other microstructural inconsistencies with beamlines achieving a voxel size of the order of $1 \mu\text{m}^3$, depending on experimental setup, equipment and

Table 1
Material properties of Alloy 2205 duplex stainless steel [52].

Property	Value
Density [kg/m^3]	7700
Young's modulus [GPa]	190
Poisson's ratio	0.3
Yield stress [MPa]	450

Table 2
Alloy 2205 duplex stainless steel chemical composition [52].

C	Cr	Ni	Mo	N	S
0.020	22.1	5.6	3.1	0.18	0.001

the size of the sample being investigated [47]. For neutron CT the spatial resolution is heavily influenced by beam divergence and detector characteristics, such as scintillator thickness [28,29] but the resolution is often of the order of tens of micrometres. However, neutrons have the benefit of deeper penetration in engineering materials compared to X-rays. Hence engineering materials with relatively high atomic numbers, such as steels, are significantly more suited to NCT than XCT. Isotope-specific imaging is another advantage offered by NCT. For example, NCT has been used to observe the distribution of hydrogen, which heavily scatters neutrons, within as-received steel plates, to develop materials resistant to hydrogen embrittlement [30,31]. Time-of-flight neutron imaging may also be used to identify contrast between phases, if they have differing crystalline structures. For instance, if one phase has a body centred cubic (bcc) crystalline structure, and the other has a face centred cubic structure (fcc), the transmitted neutron spectra will vary, hence both neutron and X-ray CT have been used in this study.

3. Experimental design

3.1. Sample material, geometry, and initial fatigue study

Alloy 2205 duplex stainless steel was used in this study. It consists of Body Centre Cubic (bcc) ferritic α and Face Centre Cubic (fcc) austenitic γ phases in roughly equal volume fractions. The typical material properties can be found in Table 1, with chemical composition displayed in Table 2 [52]. Electron backscatter diffraction was performed on a cross-section of the material, revealing that there was stronger texture in the ferritic phase compared to the austenite (Fig. 2).

A cylindrical sample was used as it has been shown that the 3D elastic stress field in an axisymmetric sample can be back calculated from through thickness average energy dispersive strain measurements [45,46]. The sample geometry is shown in Fig. 3; a notch was machined so that the location of the fatigue crack is prescribed to facilitate continuous monitoring using Bragg edge transmission imaging. The notch dimension was $a/W = 0.2$ ($a = 1 \text{ mm}$, $W = 5 \text{ mm}$).

It was important to ensure that a crack initiated within a known number of cycles that could fit in the tight schedule of the beamtime. It was therefore essential to select a load that induced failure within the order of several hundred thousand cycles as the test frame could reliably apply fatigue load up to 10 Hz. The total number of test specimens available for preliminary investigations was restricted to seven due to shortage of material. Whilst ten samples were machined in total, three were retained for the in situ experiment, to ensure one test specimen and two spares were available if a sample were to be accidentally damaged during setup. In order to identify the appropriate load, a number of specimens were tested before the neutron experiments at different levels of load and their fatigue lives were measured; these can be seen in Fig. 4. An initial maximum load, P_{max} , for preliminary testing was estimated by applying the Point Method approach to the Theory

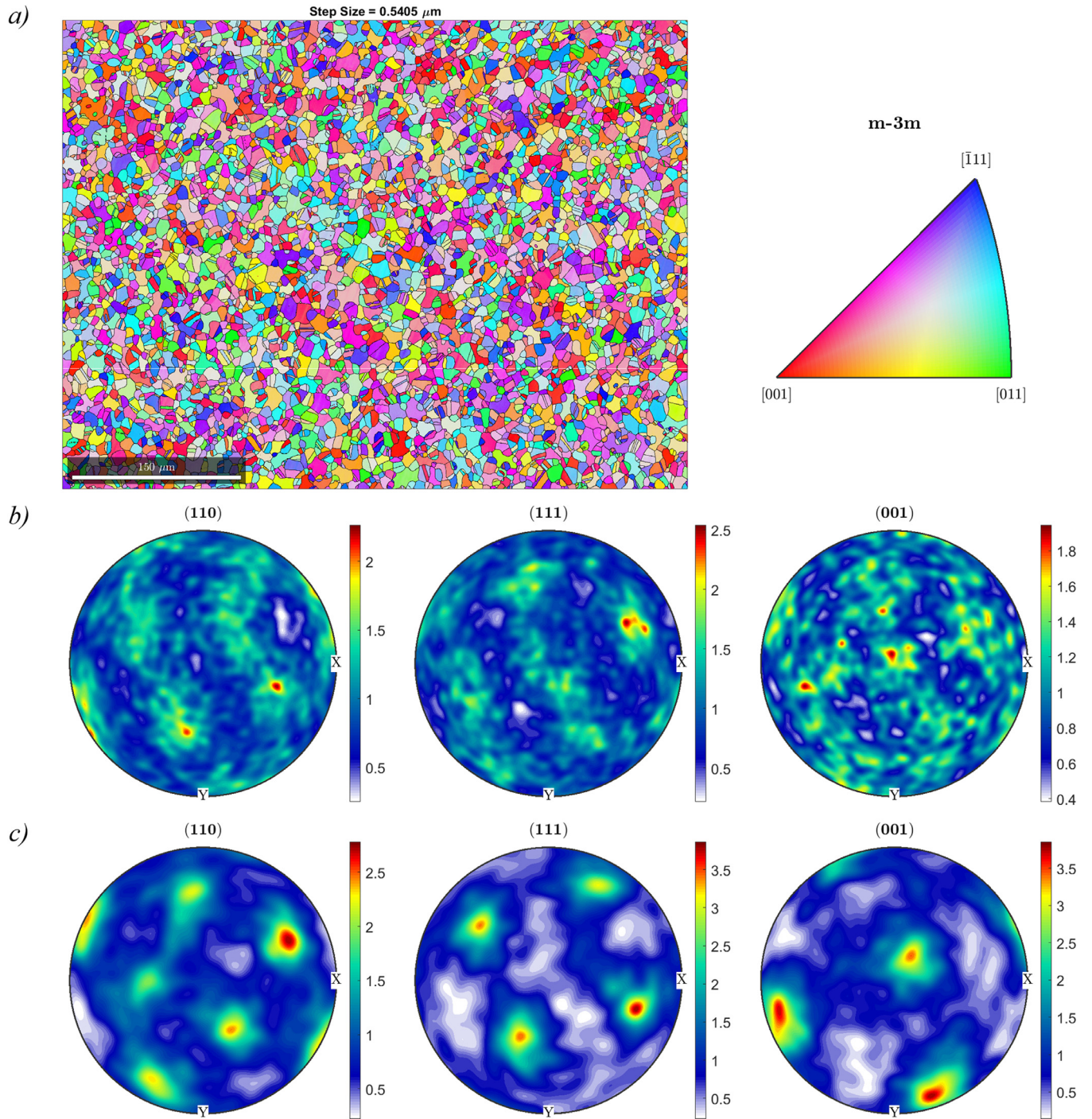


Fig. 2. EBSD results: (a) The grain-boundary energy distribution (GBED) and corresponding key for Alloy 2205 duplex steel, performed with a step size of 0.5405 μm . (b) Orientation distribution function for austenite. (c) Orientation distribution function for ferrite.

of Critical Distances [55], which estimated that a maximum load of approximately 11 kN would be required to damage the sample within the medium cycle fatigue regime at roughly 5×10^5 cycles. This proved to be conservative and based on the results depicted in Fig. 4, a maximum applied load of 16 kN would be used for the in situ loading experiments. Using assumptions from Linear Elastic Fracture Mechanics, the fatigue life of the sample was estimated to be less than 869,000 cycles, keeping within the dedicated experimental beamtime [31,56,57]. In all tests $R=P_{\min}/P_{\max}=0.01$ was selected as it often provides the closest agreement with the theory of critical distances and the tests were carried out on an Instron 50 kN servo-hydraulic test frame at 10 Hz.

3.2. In situ loading Bragg edge transmission neutron imaging

The in situ loading neutron transmission imaging experiment was conducted using a 50 kN hydraulic Instron load frame at the ENGIN-X instrument at the ISIS Neutron and Muon Source, Rutherford Appleton Laboratory, UK. The sample was fatigued at maximum load of 16 kN in displacement control, with $R=0.01$ and frequency of 10 Hz. Local compliance of the sample around the notch was measured before each scan using an extensometer of gauge length 12.5 mm attached to the specimen. Crack nucleation would increase the compliance of the sample thus allowing an independent method to detect the crack. Similarly,

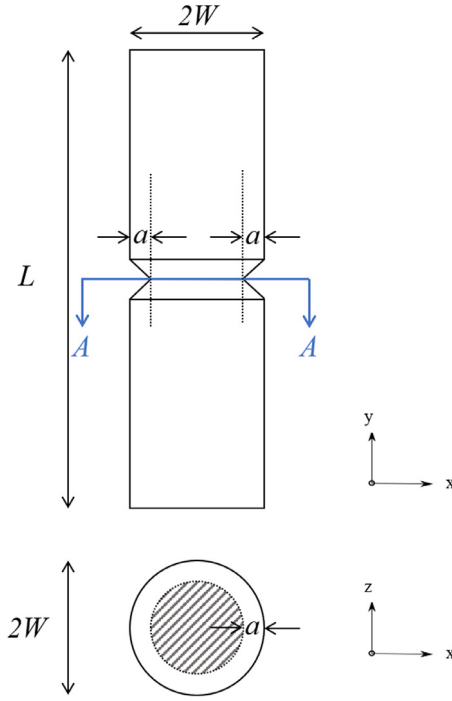
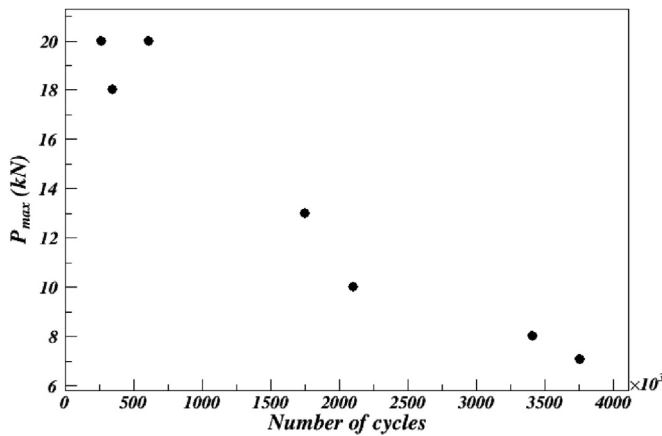


Fig. 3. Schematic of sample geometry.

Fig. 4. Fatigue life of seven samples, preliminarily tested to estimate a load at which the sample could fail in a reasonable number of cycles. $R = 0.01$.

peak-to-peak loads were continuously measured and monitored visually as crack nucleation would result in a drop in the load allowing for further validation.

Peak-to-peak load monitoring was achieved using a high frequency load cell with the output signal recorded using a National Instrument data acquisition system at 10 kHz. Load data was concurrently analysed using an in-house python code, providing graphical visualisation of the peak-to-peak load variation every 250 cycles. Cyclic loading of the sample was paused, with the sample held at maximum load, to allow for completion of Bragg edge imaging scans at 0, 2.5×10^5 , 3.5×10^5 , 4.5×10^5 and 5.145×10^5 cycles. A microchannel plate (MCP) neutron counting detector, designed by Nova Scientific and University of California at Berkeley, was used to obtain two-dimensional radiographs, details of which can be found elsewhere [19–37]. The MCP comprised a 2×2 array of Timepix readout application specific integrated circuits (ASIC), with 512×512 pixels each $55 \times 55 \mu\text{m}^2$ providing a total field of view (FoV) of $28 \times 28 \text{ mm}^2$ [59]. On detection of a neutron, an electron avalanche is generated within the MCP pore that is subse-

quently counted by the ASIC readout CMOS chip, along with the neutron ToF. For the cold and thermal neutron energies, detection efficiency is approximately 50% [60], with a selected time resolution of 4.48 μs [38–40].

As the MCP has been designed for a different beamline (the IMAT facility) and not for the ENGIN-X beamline, a custom-built mounting arrangement was used to ensure that the distance between sample and detector was minimised, reducing the negative impact of geometrical blurring. The setup, seen in Fig. 5, enabled a sample to detector distance of 25 mm. The measured ToF range, between 5 ms and 68.3 ms, was chosen to ensure that Bragg edge positions of the most useful hkl planes with highest intensities, for example the 110 and 111, were captured. A flat field scan, without a mounted sample present, was recorded to normalise the scans for varying pixel response and non-uniformity of the beam.

ENGIN-X, a beamline dedicated to strain measurement, is designed for a high ToF resolution which negatively impacts its neutron flux. Conversely, IMAT a dedicated imaging beamline, has much higher flux but at the time of the experiment, was not capable of housing the 50 kN Instron load frame. The experiment, therefore, had to be carried out at ENGINX which meant significantly longer scan times than what is expected from an imaging beamline. A preliminary scan was performed on the sample, with the quality of counting statistics being checked every hour, to ensure that spectral data was satisfactory in all regions of the sample, regardless of the varying material thickness. It was determined that 4-hour scans allowed for adequate acquisition statistics. Fig. 6 shows an example transmission spectrum for the duplex steel specimen, with certain Bragg edges and their associated crystallographic phases (α or γ) exhibited.

The analytical function previously detailed (Eq. (2)) was used to fit Bragg edges and their associated wavelength λ was extracted for each pixel, allowing for generation of two-dimensional maps examples of which will be given in Section 4.3. The residual stress of the as-manufactured specimen was not the focus of this study thus, a stress free specimen to determine the stress free Bragg edge wavelengths (i.e. d_0) was not examined [20]. The values of λ_0 were obtained at a region away from the notch prior to cycling. Due to the relatively low flux available at neutron facilities, an individual pixel has a low signal-to-noise ratio [62]. Nevertheless, counting statistics were improved substantially by employing a spatial binning technique, at the sacrifice of effective spatial resolution [41,42]. Analysis was completed pixel by pixel, whilst recursively combining spectral information from a 39×39 pixel region, ensuring sufficient statistics were available to fit the Bragg edges.

3.3. Neutron tomography

After the in situ experiment, a neutron computed tomography (NCT) scan was performed on the sample on the IMAT imaging beamline. The specimen was positioned 11 mm from the 2048×2048 pixel AN-DOR Zyla CMOS 4.2 Plus detector [48]. The imaging camera does not distinguish between the differing neutron energies, generating white-spectrum radiographies. For neutron CT, spatial resolution is dominated by geometrical blurring because of sample positioning, which is in turn dependent on the instrument specific beam divergence, referred to as the L_B/D_B value. This value is calculated using the equation:

$$\frac{L_B}{D_B} = \frac{l_{max}}{d_B} \quad (6)$$

where, L_B is the distance between the beam focusing aperture and the camera (10 m), D_B is the aperture diameter (40 mm), l_{max} is the maximum distance between the sample and the camera (23 mm), whilst d_B is the geometrical blurring. The setup for NCT scans equated to geometrical blurring that provided a spatial resolution of approximately 92 μm . The Nyquist-Shannon sampling theorem postulates that the minimum number of projections (N) required for a 360° rotation of the samples is

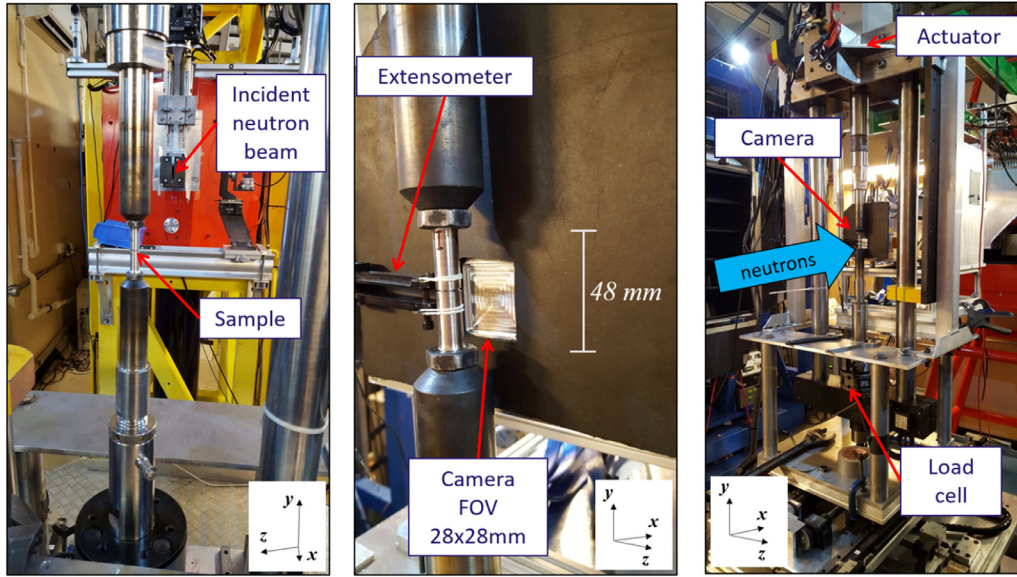


Fig. 5. Experimental setup, demonstrating the sample position in relation to the incident neutron beam and the MCP detector.

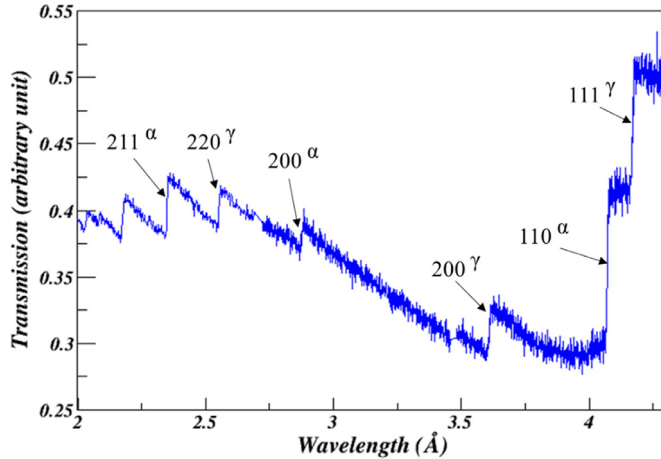


Fig. 6. Transmission spectrum for Alloy 2205 duplex stainless steel. The individual hkl planes have been labelled with reference to their associated allotrope, ferrite α -phase and austenite γ -phase.

calculated for cylindrical samples using the equation [64]:

$$N = \frac{W \times \pi}{d_B} \quad (7)$$

where, W is the sample radius. It was calculated that $N=204$ would be sufficient, each projection count time was thus 30 s, with rotations of 1.76° between each scan. Open beam scans (flat field), without the presence of a sample, were taken before and after each tomography to normalise pixel-to-pixel variations in sensitivity and the influence of fluctuations in beam intensity across the detector FoV. Dark scans (dark field), with the shutter closed, were taken before the first and after the final tomography to correct for electronic noise within the detector. Also, scans were performed at 180° and 360° to correct for sample tilting.

Once the projections are recorded, they were reconstructed to produce a three-dimensional representation of the specimen. Neutron tomography data is significantly noisier than X-ray tomography due to a lower signal to noise ratio. For such datasets, the simultaneous algebraic reconstruction technique (SART) is preferred to other forms of conventional reconstruction algorithms such as filter back projection (FBP) [65]. SART is an implementation of the frequently applied itera-

tive technique, ART [31,42–66], yet only requires one single iteration, significantly reducing the necessity of computational power. The FBP and SART algorithms were both used to reconstruct the NCT datasets to allow for comparison.

3.4. X-ray computed tomography

A synchrotron X-ray computed tomography (XCT) scan was also recorded on the sample at Beamline I12 (JEEP), Diamond Light Source, UK [47]. As the X-ray attenuation coefficients for the ferrite and austenite phases are very close ($<3\%$), the scan was not expected to reveal any other microstructural information on the different phases in the duplex steel. The X-ray CT scan used a 90 keV monochromatic parallel beam and the beamline's custom imaging detector, consisting of a 2560×2160 pixel PCO.edge sCMOS detector lens-coupled to a LuAG:Ce scintillator. The nominal pixel resolution was $7.91 \mu\text{m}$. A total of 1800 projections over 180° were captured with an exposure time of 4.5 ms per projection.

Reconstruction of the X-ray CT data was completed using the Fourier based *gridrec* algorithm [67]. This method provides significantly higher quality images on well sampled tomographic data sets, when compared to the conventional filtered back projection (FBP) algorithm [67].

3.5. Scanning electron microscopy

After the non-destructive methods were used to evaluate the crack initiated in the specimen during in situ loading experiments, the sample was destructively tested to validate the non-destructive observations. The sample was cooled in liquid nitrogen below its ferrite phase ductile to brittle transition temperature and pulled in tension using the Instron loading frame at ENGIN-X. This created a final fracture surface that was distinctly different from the fatigue crack surface developed during the in situ cyclic loading experiment, therefore allowing the fatigue crack geometry to be studied. The fracture surface was examined using JSM-6610LV low vacuum scanning electron microscope (SEM), at the Research Complex at Harwell (RCAH), UK.

3.6. Finite element analysis

Once a fatigue crack nucleates, the stress field in the sample changes to accommodate the reduction in the uncracked ligament as well as the stress concentration around the crack front. To calculate the strain field

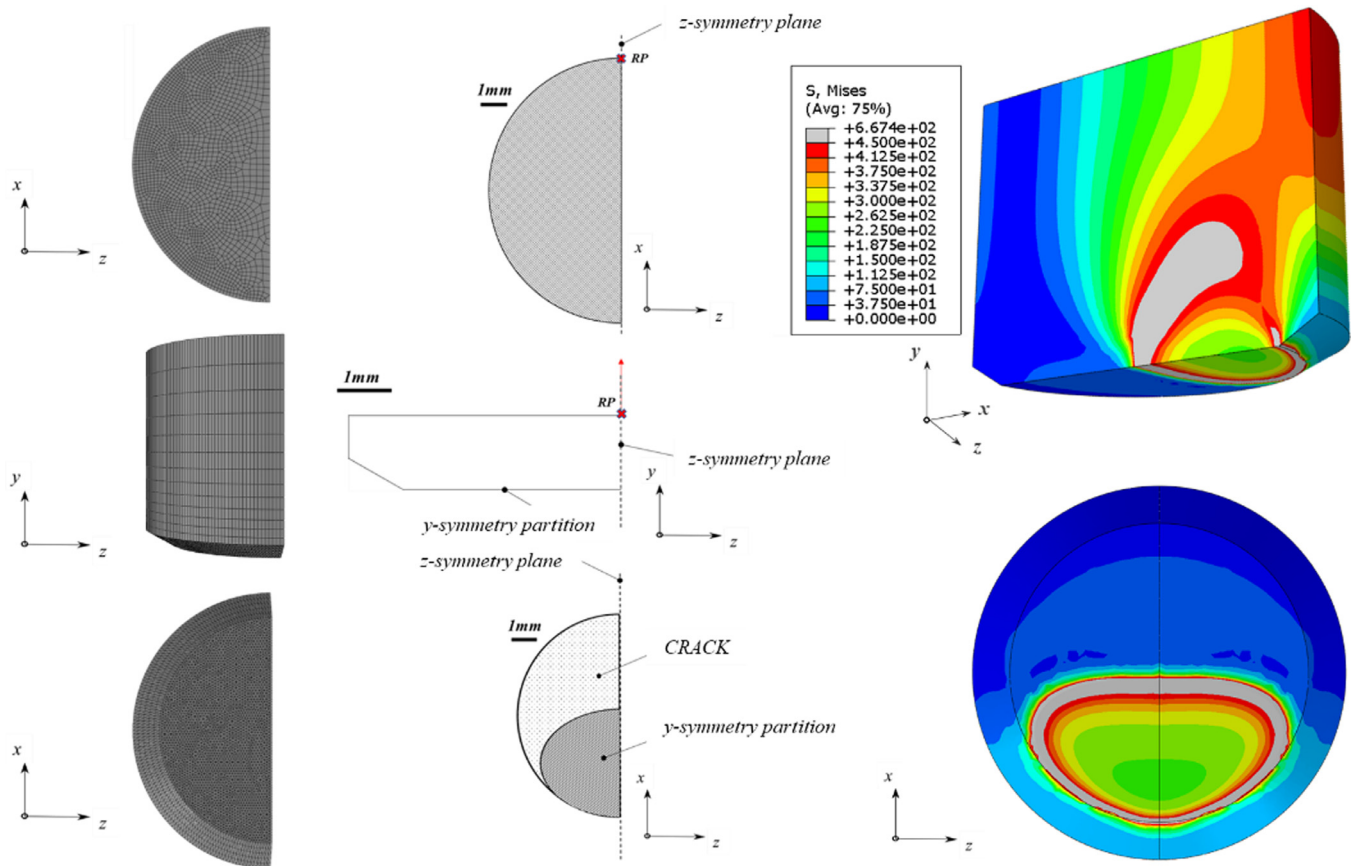


Fig. 7. Schematic of the finite element model used to examine theoretical elastic strains in the cracked sample, assuming symmetry to simulate the crack geometry, as viewed by SEM. (Left) Mesh, (Middle) symmetry and loading conditions, (Right) examples von-Mises stress distribution from the FEA results in 3D and cross section.

expected in a cracked sample, ABAQUS version 6.14–2 [68] was used to develop a static three-dimensional elastic-plastic model. The crack geometry as viewed by SEM (see Section 4.2) was simulated in the model. A schematic of the model can be seen in Fig. 7. Mesh refinement was completed in the region of interest, surrounding the crack and the notch, using a mesh size of 0.1 mm, quadratic tetrahedron elements (C3D10). Since there was no unloading simulated, no particular specification on the type of hardening for the plastic behaviour of the material was required, thus isotropic hardening was assumed. The material properties used (Table 1) obtained in prior work [69]. A quarter of the sample was modelled, taking advantage of the sample's symmetry in the z-axis. Symmetry in the y-axis was included to simulate the presence of the crack, through applying symmetry boundary conditions on a partitioned region of corresponding geometry to the crack, as viewed with the SEM. The boundary condition allows for the rotation of the cross-section plane induced by the combined tension and bending of the cracked sample to be simulated. A concentrated load was applied through a single reference point that was distributed across the top of the sample, as it was assumed that this would best simulate the influence of a bending moment induced by a substantial crack whilst under tensile load.

4. Results

4.1. Fatigue life of test specimen

The cyclic loading was paused during the experiment and scans were performed at 0 , 2.5×10^5 , 3.5×10^5 , 4.5×10^5 and 5.145×10^5 cycles. A sudden drop in the peak-to-peak load was observed at roughly 5.0×10^5 cycles (see Fig. 8), with a crack at the notch becoming visible by eye at 5.145×10^5 cycles. From the peak-to-peak load, it could be suggested

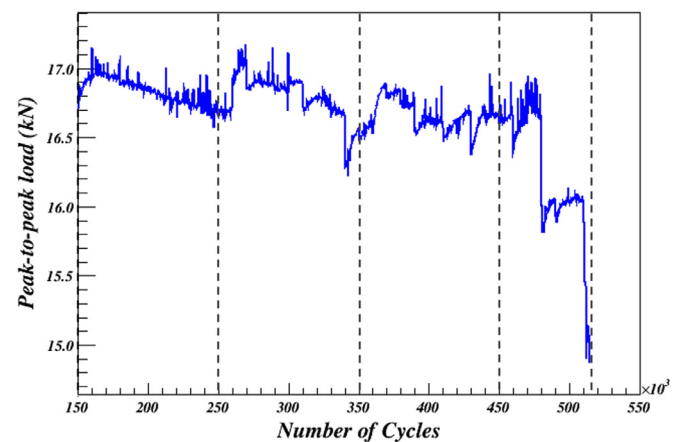


Fig. 8. Peak-to-peak load versus the number of cycles. The dashed lines indicate when fatigue loading was paused to complete a neutron transmission scan, with the sample held at the maximum load.

that a crack was nucleated earlier at 1.6×10^5 cycles (note the gradual peak-to-peak drop), or possibly just before 350,000 cycles (note the significant and visible peak-to-peak drop).

4.2. Fractography

Fig. 9 shows the SEM images taken from the fracture surface of the sample. The specimen has lost its circular cross section, which indicates some deformation has occurred whilst destructively pulling the sample

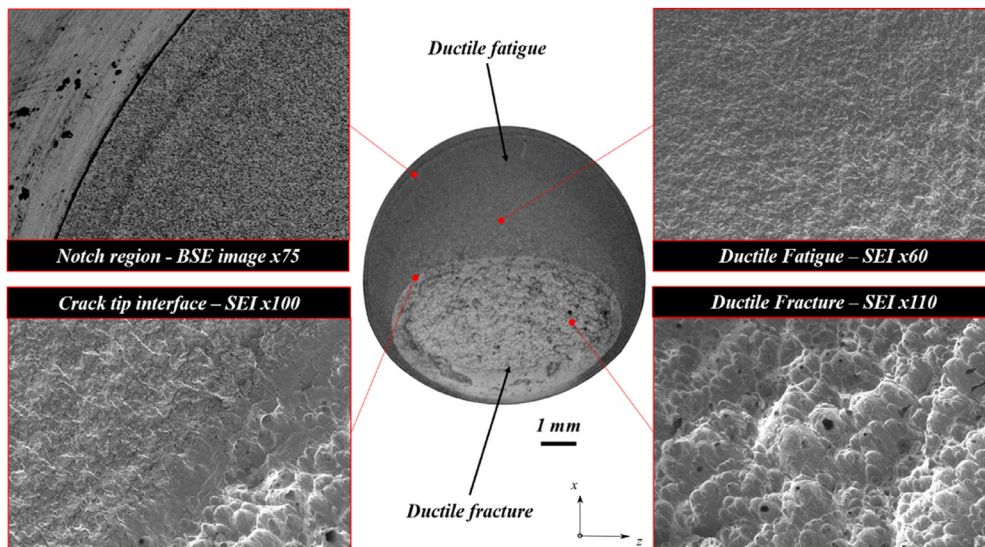


Fig. 9. (Centre) X13 Image of crack topology, which no longer appears circular due to deformation during the pulling process. (Clockwise from top left) X75 BSE image of proposed crack initiation site; X60 SEI of ductile fatigue region close to the notch; X110 SEI of the ductile fracture region; X100 SEI of crack tip region.

apart. The fatigue crack growth region is clearly visible as a smooth area typical of ductile fatigue; the final shape of the crack front is obvious in the central image. The large fatigue failure area is accompanied by the rough area (bottom right figure), characteristic of ductile fracture. The interface between these two regions (bottom left) signifies the final crack front during the in situ experiment. The crack has propagated in an asymmetric fashion, which is potentially related to slight misalignment of the Instron loading frame used during the in situ experiment.

4.3. In situ energy dispersive neutron imaging

The $bcc \{110\}_\alpha$ and $fcc \{111\}_\gamma$ lattice planes were used to measure strain in the ferritic and austenitic phases of the duplex steel respectively at peak load. As seen in the materials transmission spectrum (Fig. 6), the height of both edges are significantly greater than any other Bragg edges in each phase. Most importantly, the $\{110\}_\alpha$ and $\{111\}_\gamma$ plane families have both previously been used successfully to measure strain, demonstrating reasonable agreement with bulk elastic response [34,70].

Fig. 10 shows the elastic strain maps and the elastic strain along the notch for both hkl planes $bcc \{110\}_\alpha$ and $fcc \{111\}_\gamma$ at various intervals throughout the cyclic loading. It should be noted that the full field beam measures the average strain through the thickness of the specimen, which varies due to its circular cross section across the map. These results demonstrate the crack may have nucleated prior to 250,000 cycles, as the strain visibly increases relative to pre-loading. Also, there is a distinctive strain redistribution when the fatigue crack has propagated to a significant size at 514,500 cycles. The effect of the fatigue crack can be identified more clearly in the ferritic $\{110\}_\alpha$ elastic strain maps compared to the corresponding austenitic $\{111\}_\gamma$ maps. For both maps generated at 514,500 cycles, the region associated with crack tip stresses, which appears to have contributed most significantly to the clear strain redistribution has been labelled, localised crack tip stress. Analysis of ferritic strain partitioning between the ferrite and austenite phases of the duplex steel was not the primary objective of this study. However, it can be seen in the maps that the ferrite phase is carrying more of the strain in the material. This is in agreement with previous studies on duplex stainless steels, which demonstrated stiffness in the ferrite is generally greater than in the austenite [71]. The diffraction elastic moduli of $\{110\}$ and $\{111\}$ are 242 GPa and 214 GPa respectively [72] which along with strong texture typically observed in wrought duplex stainless steels [73] can account for the strain partitioning observed in the measurements. The error of measured strain corresponds to uncertainty in determining the Bragg edge position, like strain measured using Bragg peak analysis. The Bragg edge fitting error in the strain map generation is 3.82×10^{-4} for $\{110\}_\alpha$ and 4.29×10^{-4} for $\{111\}_\gamma$. This translates to

strain errors of roughly $94 \mu\epsilon$ and $103 \mu\epsilon$ for $\{110\}_\alpha$ and $\{111\}_\gamma$, respectively.

Small regions of extremely high compressive stress, with some examples labelled ‘non-converging pixels’, correspond to areas where it has not been possible to fit the Bragg edge. This occurs more frequently in the $\{111\}_\gamma$ data, particularly at 0 cycles and after the crack has been nucleated at 514,500 cycles. This also suggests that strain in the austenitic material is more difficult to study for duplex steels, as maps for both edges at each number of cycles are generated from the same data set. The presence of plasticity will generate high intergranular strains, known to impact strain measurement accuracy [74]. Yet this effect is assumed to be negligible as the influence of localised plastic strains, associated with crack tip stresses, will have diminished on averaging through the entire material thickness.

4.4. Post-fatigue CT imaging

Fig. 11 displays reconstructed slices from neutron and X-ray tomography scans. The virtual slices of NCT were obtained using FBP and SART algorithms with and without a median 3×3 filter. Fig. 11 also demonstrates the values of signal to noise ratio (SNR) and contrast to noise ratio (CNR) for each algorithm used for NCT reconstruction. CNR and SNR were calculated using a slice 40 mm from the notch and Eqs. (8) and (9) [66–75]. The visual inspection of the reconstructed slices, presented in the Fig. 11, appears to demonstrate that SART is the favoured algorithm for the noisy neutron data set. This is confirmed by the CNR and SNR values. Background noise is further reduced on application of the filter, again supported by higher SNR and CNR. For context, the X-ray reconstruction SNR and CNR values were 42940 and 579, respectively.

$$SNR = \frac{\mu_{sig}}{\mu_{bg}} \quad (8)$$

$$CNR = \frac{\mu_{sig} - \mu_{bg}}{\sigma_{bg}} \quad (9)$$

where, μ_{sig} and μ_{bg} are mean pixel value for the signal area (inside the sample) and background area (outside the sample), whilst σ_{bg} is the background area’s standard deviation.

Volume rendering of both reconstructed data sets was completed in Avizo 9.3.0 software [76]. The better spatial resolution of XCT ($\sim 7.91 \mu m$) offers a greater opportunity to examine the crack morphology compared to NCT which has poorer spatial resolution ($\sim 92.0 \mu m$). It was therefore more difficult to visualise the crack using NCT. Using the filtered SART reconstruction algorithm for NCT reconstruction, however, it was possible to distinguish the crack. The side-by-side

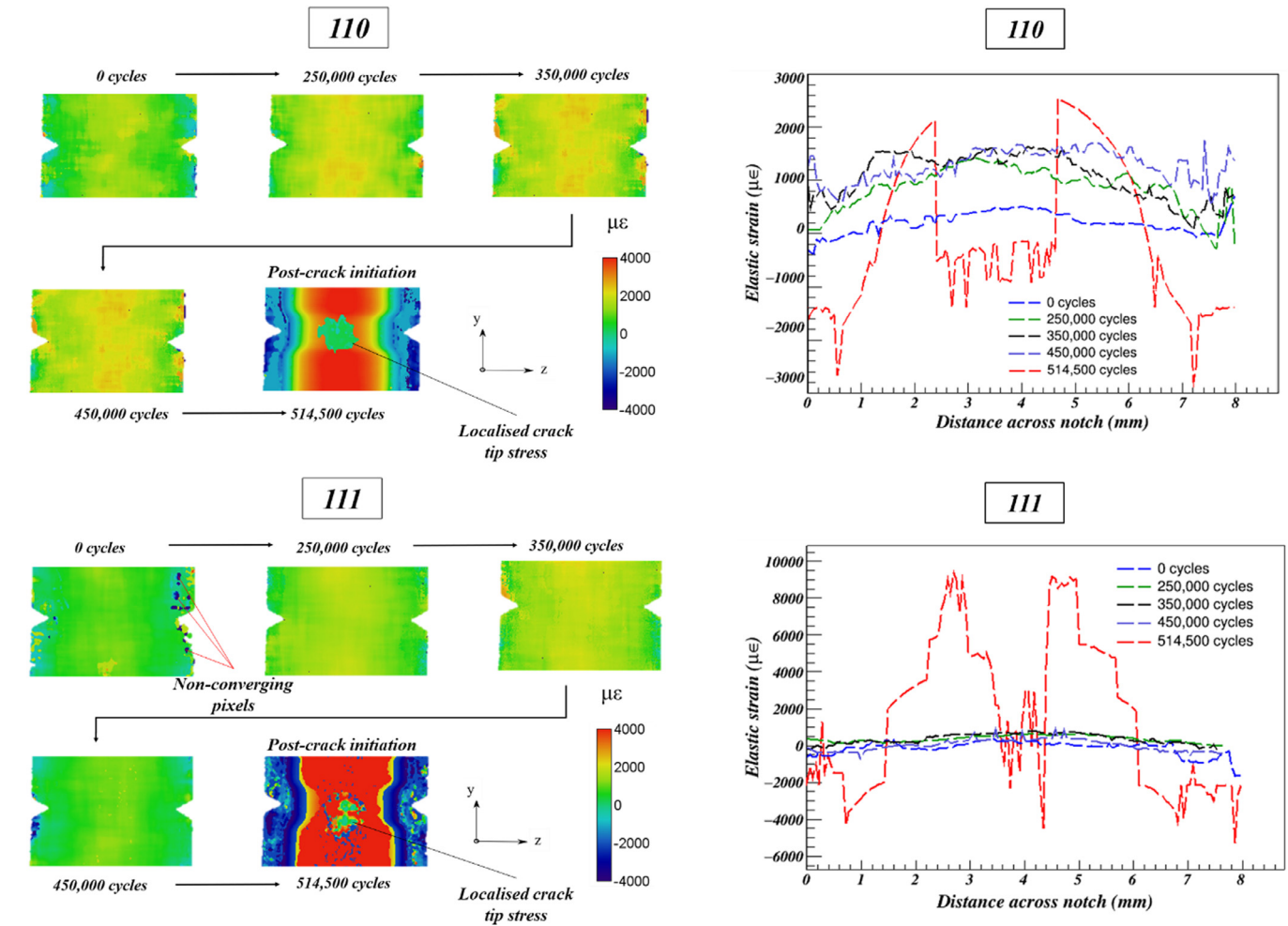


Fig. 10. (Left) The elastic strain maps generated using the ferritic 110 and austenitic 111 planes, at six points through the samples fatigue life. The strain gradually increases as the crack propagates and the cross section reduces. (Right) Graphical representation of the elastic strain measured along the notch, supporting crack nucleation may have occurred prior to 250,000 cycles. The final scan at 514,500 cycles clearly demonstrates the expected redistribution of stress associated with a crack of significant size. The compressive strain observed in the final stage is due to out of plane bending of the sample as the crack propagates non-symmetrically.

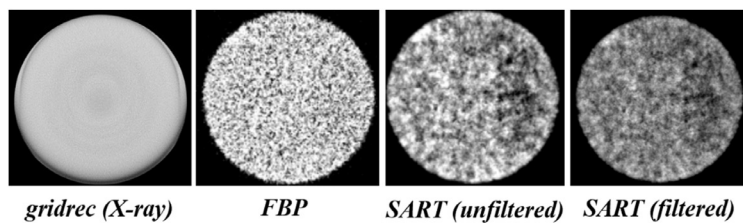
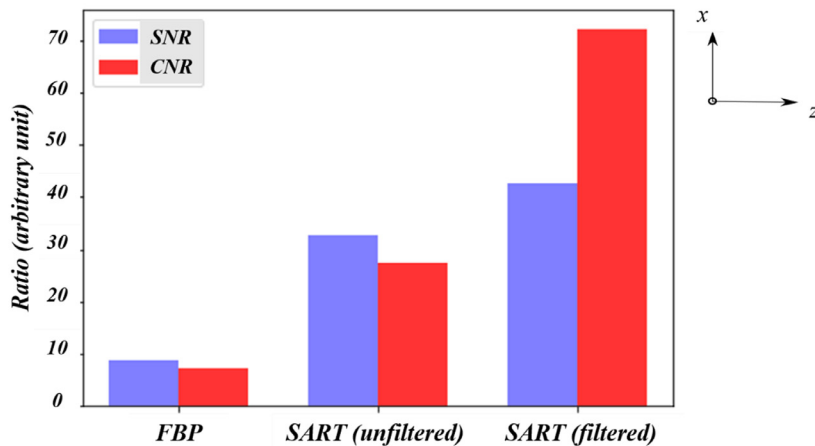


Fig. 11. (Top) Reconstructed slices of the X-ray data using the gridrec algorithm, with FBP and SART algorithms for neutron data. Slices were all taken 40 mm from the notch, to ensure the crack did not influence results. (Bottom) Quantitative representation of neutron reconstruction qualities using their SNR and CNR.



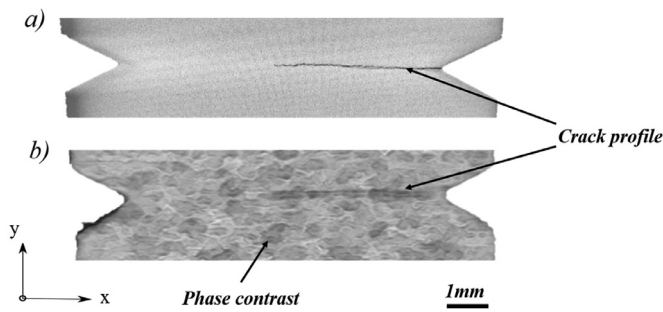


Fig. 12. Slice from rendered X-ray CT (a) and neutron CT (b) at the same location, allowing for direct comparison of the techniques regarding their ability to visualise the crack profile.

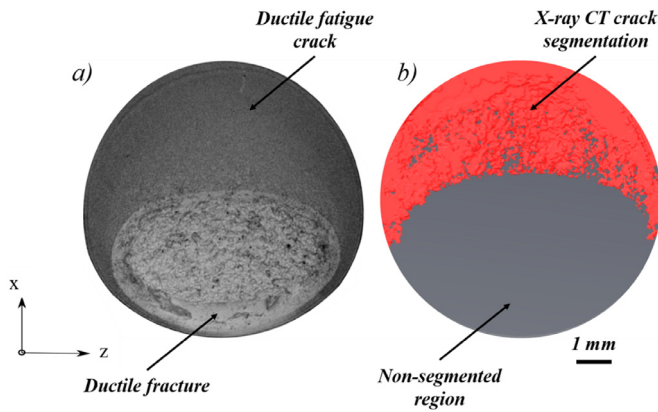


Fig. 13. The crack as seen using (a) SEM – note the distortion that occurred whilst pulling the sample apart; (b) by segmenting the crack using X-ray CT. This is the area over which the neutron Bragg edge tomography measures average strain.

comparison of XCT and NCT crack profile in Fig. 12 confirms this. The X-ray reconstruction shows a clear crack outline, due to the high spatial resolution of X-ray tomography, and with significant attenuation contrast between steel and air, confirming the shadow witnessed in the neutron image is caused by the crack.

The X-ray absorption behaviour is considered the same for both phases but it is apparent that the NCT can provide information on the duplex steel phases, as there is visible contrast as a result of the austenite and ferrite. Whilst localised microstructural features, such as carbides, are certainly present in the material, it is unlikely that they would greatly influence the NCT image quality, as their size is generally much smaller than that of the technique's spatial resolution [77]. Fig. 12b demonstrates how it is possible to examine the internal variations in phase, and potentially with improved resolution allow for the development of a range of post-processing correlative techniques, to be discussed in Section 5. This variation in the greyscale offers a chance to analyse the NCT data using digital volume correlation if the before and after loading volumetric images were available.

Fig. 13 compares the fractographical crack topography seen using SEM with the crack morphology observed in a cross-section of the rendered and segmented XCT data. Crack segmentation using the rendered neutron data was not possible as there was insufficient contrast between the crack and surrounding metal. Comparing the segmented XCT and SEM images allows for valuable insight into the limitations in most accurate non-destructive (i.e. XCT) and destructive methods. Whilst the morphology of the crack in both images are very similar, it appears that regions close to the crack tip have been omitted in XCT data as the opening of the crack was less than the spatial resolution of the tomography data.

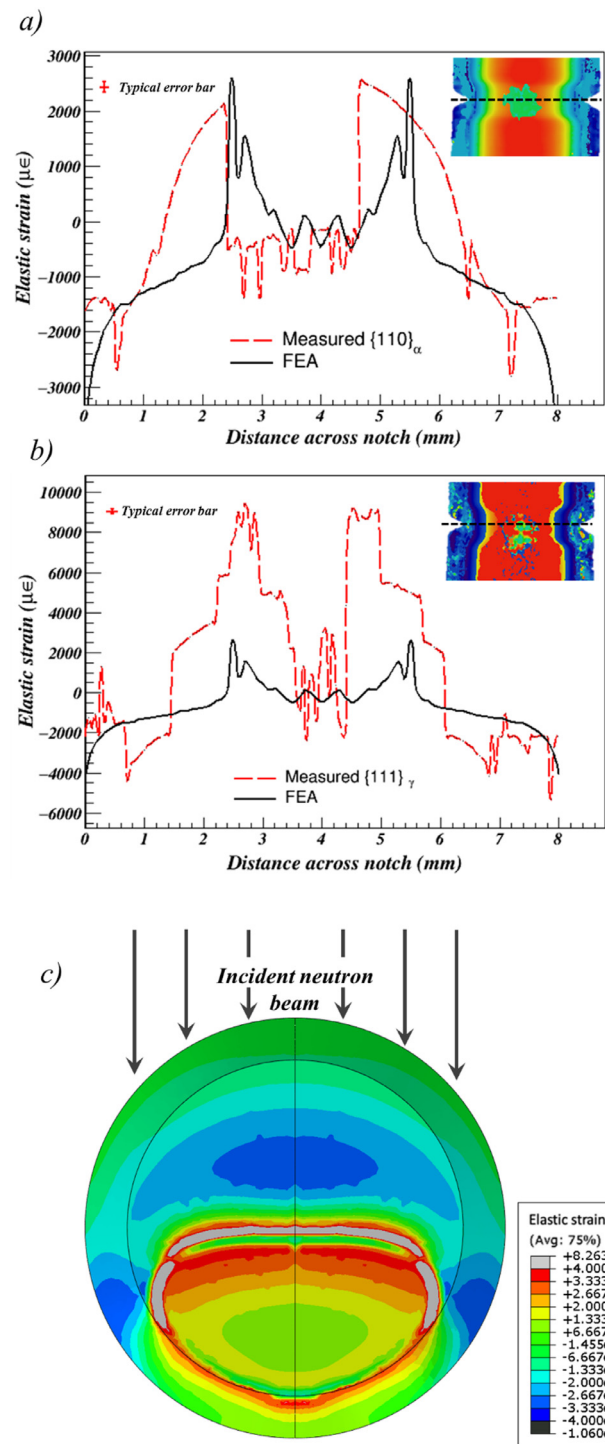


Fig. 14. (a) Comparison of measured $\{110\}_\alpha$ and FEA elastic strain running parallel to the notch for the cracked sample. (b) Comparison of measured $\{111\}_\gamma$ and FEA elastic strain running parallel to the notch for the cracked sample. Inset on both graphs is the corresponding strain map. Typical $\mu\epsilon$ error corresponding to the Bragg edge fitting error for the 39×39 pixel spatial binning used for strain map generation. (c) Elastic strain from FEA on the cracked cross section of the sample with assumed beam direction relative to the crack.

4.5. Finite element analysis

Bragg edge imaging measures average through thickness elastic strain. Therefore, the same through thickness averaging on the elastic component of strain was performed on the FE results. This averaging takes into account the higher stress field around the crack tip as well

as the bending stress that is induced in the sample due to the crack invalidating the initial axisymmetric condition of the sample. No differentiation between the phases were considered in the model, and the macromechanical material properties of the duplex steel were considered. Fig. 14 shows the comparison between the FE results and measurements made on $\{110\}_\alpha$ and $\{111\}_\gamma$ along a profile passing through the centre line of the notch. Fig. 14 shows a good agreement between the FE results and the experimental measurements although $\{110\}_\alpha$ measurements are closer to the model than $\{111\}_\gamma$, which could be explained by the significant difference in levels of texture between the two phases.

5. Discussion and future work

5.1. Discussion

The aim of this investigation was to detect and quantify the effects of a crack using various non-destructive techniques: neutron Bragg edge transmission imaging, neutron computed tomography, X-ray computed tomography. The non-destructive findings were validated against a destructive scanning microscopy analysis. Bragg edge transmission imaging was demonstrated to identify the presence of a crack in situ, through the generation of strain maps. Although a quantitative method that measures the average strain through the sample, Bragg edge imaging is incapable of resolving crack morphology. Alternatively, it was shown that neutron tomography can be used to create a three-dimensional representation of the crack in the sample as well as observing contrast in the duplex stainless steel specimen due to its two different phases. X-ray tomography has a much higher spatial resolution, which could be used to segment the crack in a volumetric image more precisely. However, the low penetration depth of X-ray in engineering materials such as steel can be limiting. It is also not possible to resolve different phases of duplex steel in X-ray absorption contrast tomography due to the similarity between their attenuation coefficients. Other techniques such as X-ray propagation phase contrast tomography might be used for this purpose [78].

The specimen was designed to be axisymmetric so that the strain field across its cross section could be back-calculated from the through thickness average strain measured using the full field beam in the Bragg edge imaging experiment. The crack propagated unsymmetrically through one side of the specimen invalidating its axisymmetric condition. It was therefore not possible to back-calculate the strain variation through the cross-section analytically. Instead, a three-dimensional finite element model was created whose crack geometry was representative of that observed in the scanning electron microscopy study.

It was also concluded that strain accuracy is significantly better for the ferritic $\{110\}_\alpha$ edge, than that of the austenitic $\{111\}_\gamma$ edge. The NCT technique also demonstrates the presence of a crack, yet is restricted by lower spatial resolutions, especially when compared to the more conventional XCT. Both neutron imaging techniques hold great promise, with the potential to be used in conjunction with each other for correlative studies.

Directly compared with X-ray computed tomography, the neutron computed tomography appears to be lower in quality, as seen in Fig. 12. It was observed that NCT has the ability to distinguish different phases in the duplex steel, potentially providing an opportunity to be used with quantitative three-dimensional strain measurement techniques such as DVC. Despite having a greater spatial resolution, the XCT cannot resolve near-tip crack morphology when the sample is unloaded. This is likely due to the crack closure after unloading. It has been shown that for accurate observation of cracks, in situ loading experiments that keeps the crack open are more successful [79].

Finite element analysis of the sample was performed which included information from the crack morphology obtained using SEM analysis. Strain measured in the ferritic $\{110\}_\alpha$ is of a comparable order of magnitude to that of the FEA, with a clear drop when averaging entirely along the crack tip, similar the FEA. The austenitic $\{111\}_\gamma$ edge measures un-

realistic magnitudes of strain, and whilst the maps provide evidence of a crack, the strain measurements are less accurate.

The differences between the strains that are measured experimentally and calculated by FEA are likely to be caused by the crack front not being completely perpendicular to the beam direction, which was assumed when modelling. The neutron transmission scan was performed with the crack opening being very nearly perpendicular to the incident beam, yet even small misalignments can cause noticeable shifts in the relative crack position, as seen in the strain cross-section. The scan being averaged through the material thickness, however, only provides useful information because the sample is suitably orientated in a appropriate direction.

5.2. Future work

This study demonstrated the potential of Bragg edge transmission imaging for detecting the presence of cracks, through the generation of two-dimensional strain mapping. To improve counting statistics, it would be recommended to scan for longer times, which would eradicate the non-converging regions, whilst also allowing for a reduced spatial binning area and improved effective spatial resolution. The next steps for the Bragg edge technique would be development of a three-dimensional elastic strain field, by completing Bragg edge tomographic scans at many different angles. This is a technique currently under development, with the theoretical and practical issues around it being tackled by others [32,33]. Also, through the development of microstructurally informed models, for example crystal plasticity finite element modelling, it may be possible to develop a greater understanding of the difference between the strain measured in the ferritic and austenitic phases, assuming that material texture has been measured accurately.

For neutron CT, the practical aspects are current, with dedicated imaging beamlines continuously advancing the technology used to improve spatial resolution. For example, the IMAT beamline has recently introduced a cooled CCD camera, capable of reducing noise and therefore improving the quality of images. Once spatial resolutions improve enough to perform DVC, the ability to measure total three-dimensional strain should become viable using duplex stainless steel. With Bragg-edge strain mapping allowing for analysis of the elastic strain field, and neutron tomography with DVC providing the total strain full field, a combination of both techniques could give a greater understanding on crack tip elastic and plastic strain evolution.

It may also be possible to develop a correlative technique between neutron and X-ray tomography results. The crack morphology is much clearer in the X-ray images, yet it is not possible to visualise grain boundaries. The crack morphology is much less visible in the neutron images, yet the presence of phases may become clear with better spatial resolution. On registration of both volumes, it may be possible to correlate the crack and the presence of grain boundaries, providing important information on crack propagation behaviour in duplex stainless steels.

6. Concluding remarks

- Bragg edge transmission imaging can be used for generating two-dimensional maps of the average elastic strain, with spatial resolutions sufficient to see the influence of large fatigue cracks, with ferritic steel delivering better results. Spatial resolution can be improved further to get greater detailed information on localised crack tip stresses.
- Neutron CT allows for visualisation crack profiles, yet with poorer spatial resolution than that of established X-ray absorption CT. Neutron CT images do however provide information on the presence of different phases, and potentially on granular displacements, suggesting DVC is possible.

- Once both techniques reach a certain stage of development, combining results of both may allow for the study of three-dimensional plastic strain. Also, it may be possible to correlate between the information provided in neutron and X-ray tomography to further understand crack growth propagation along grain boundaries.

Acknowledgment

The author would like to acknowledge EPSRC and STFC for their support through the sponsored PhD programme (Grant number: EP/M508135/1). We thank Josef Lewis (ISIS Neutron Source) for his help with the experimental setup and Abdalrhman Mohamed (University of Oxford) for completing electron backscatter diffraction scans on the material. A Reid thanks Luca Susmel (University of Sheffield) for his insightful discussion about the Theory of Critical Distances and Philip Earp (University of Oxford) for his help on the ENGINE experiment (RB 1620213).

Data availability

All data is available with the corresponding author and provided upon request.

References

- [1] Chang JB, Hudson CM. Methods and models for predicting fatigue crack growth under random loading. *ASTM Int* 1981;748.
- [2] Lan C, Bai N, Yang H, Liu C, Li H, Spencer BF. Weibull modeling of the fatigue life for steel rebar considering corrosion effects. *Int J Fatigue* 2018;111(November 2017):134–43.
- [3] Svensson T, Hannes D, Johannesson P, Dahlberg M, Anderson A. Three HCF models for strain fatigue life of welded pipes in austenitic stainless steel. *Procedia Eng* 2015;101(C):476–84.
- [4] Jiao G, Moan T. Probabilistic analysis of fatigue due to Gaussian load processes. *Probabil Eng Mech* 1990;5(2):76–83.
- [5] Marrow TJ, Mostafavi M, Hashimoto T, Thompson GE. A quantitative three-dimensional in situ study of a short fatigue crack in a magnesium alloy. *Int J Fatigue* 2014;66:183–93.
- [6] Holford KM, Eaton MJ, Hensman JJ, Pullin R, Evans SL, Dervilis N, Worden K. A new methodology for automating acoustic emission detection of metallic fatigue fractures in highly demanding aerospace environments: an overview. *Prog Aerosp Sci* 2017;90:1–11.
- [7] Mokhtarishirazabad M, Lopez-Crespo P, Zanganeh M. Stress intensity factor monitoring under cyclic loading by digital image correlation. *Fatigue Fract Eng Mater Struct* 2018;41(10):2162–71.
- [8] Becker TH, Mostafavi M, Tait RB, Marrow TJ. An approach to calculate the J-integral by digital image correlation displacement field measurement. *Fatigue Fract Eng Mater Struct* 2012;35(10):971–84.
- [9] Bay BK, Smith TS, Fyhrle DP, Saad M. Digital volume correlation: three-dimensional strain mapping using X-ray tomography. *Exp Mech* 1999;39(3):217–26.
- [10] Gillard F, Boardman R, Mavrogordato M, Hollis D, Sinclair I, Pierron F, Browne M. The application of digital volume correlation (DVC) to study the microstructural behaviour of trabecular bone during compression. *J Mech Behav Biomed Mater* 2014;29:480–99.
- [11] Mostafavi M, Collins DM, Cai B, Bradley R, Atwood RC, Reinhard C, Jiang X, Galano M, Lee PD, Marrow TJ. Yield behavior beneath hardness indentations in ductile metals, measured by three-dimensional computed X-ray tomography and digital volume correlation. *Acta Mater* 2015;82:468–82.
- [12] Limodin N, Réthoré J, Buffière JY, Hild F, Roux S, Ludwig W, Rannou J, Gravouil A. Influence of closure on the 3D propagation of fatigue cracks in a nodular cast iron investigated by X-ray tomography and 3D volume correlation. *Acta Mater* 2010;58(8):2957–67.
- [13] Marrow TJ, Liu D, Barhli SM, Saucedo Mora L, Vertyagina Y, Collins DM, Reinhard C, Kabra S, Flewitt PEJ, Smith DJ. In situ measurement of the strains within a mechanically loaded polygranular graphite. *Carbon N Y* 2016;96:285–302.
- [14] Forsberg F, Mooser R, Arnold M, Hack E, Wyss P. 3D micro-scale deformations of wood in bending: synchrotron radiation μ CT data analyzed with digital volume correlation. *J Struct Biol* 2008;164(3):255–62.
- [15] King A, Ludwig W, Herbig M, Buffière JY, Khan AA, Stevens N, Marrow TJ. Three-dimensional in situ observations of short fatigue crack growth in magnesium. *Acta Mater* 2011;59(17):6761–71.
- [16] Takamatsu D, Yoneyama A, Asari Y, Hirano T. Quantitative visualization of salt concentration distributions in lithium-ion battery electrolytes during battery operation using X-ray phase imaging. *J Am Chem Soc* 2018;140(5):1608–11.
- [17] Wang B, Tan D, Lee TL, Khong JC, Wang F, Eskin D, Connolley T, Fezzaa K, Mi J. Ultrafast synchrotron X-ray imaging studies of microstructure fragmentation in solidification under ultrasound. *Acta Mater* 2018;144:505–15.
- [18] Leung CLA, Marussi S, Atwood RC, Towrie M, Withers PJ, Lee PD. In situ X-ray imaging of defect and molten pool dynamics in laser additive manufacturing. *Nat Commun* 2018;9(1):1–9.
- [19] Gaikwad HK, Tsvirkun D, Ben-Nun Y, Merquiol E, Popovtzer R, Blum G. Molecular imaging of cancer using X-ray computed tomography with protease targeted iodinated activity-based probes. *Nano Lett* 2018;18(3):1582–91.
- [20] Hutchings MT, Withers PJ, Holden TM, Lorentzen T. Introduction to the characterization of residual stress by neutron diffraction. Boca Raton, FL: CRC Press; 2005.
- [21] Vontobel P, Lehmann E, Carlson WD. Comparison of X-ray and neutron tomography investigations of geological materials. *IEEE Trans Nucl Sci* 2005;52(1 II):338–41.
- [22] Kockelmann W, Zhang SY, Kelleher JF, Nightingale JB, Burca G, James JA. IMAT - A new imaging and diffraction instrument at ISIS. *Phys Procedia* 2013;43(0):100–10.
- [23] Kockelmann W, Minniti T, Pooley D, Burca G, Ramadhan R, Akeroyd F, Howells G, Moreton-Smith C, Keymer D, Kelleher J, Kabra S, Lee T, Ziesche R, Reid A, Vitucci G, Gorini G, Miceli D, Agostino R, Formoso V, et al. Time-of-flight neutron imaging on IMAT@ISIS: a new user facility for materials science. *J Imaging* 2018;4(3):47.
- [24] Johannson J. Residual stresses and fatigue in a duplex stainless steel; 1999. no. 779.
- [25] Polák J. Cyclic plastic response and fatigue life of duplex and superduplex stainless steels; 2005. p. 280–9.
- [26] Chai G, Peng RL, Johansson S. Fatigue behaviors in duplex stainless steel studied using in-situ SEM/EBSD method. In: *Proceedings of the 20th European Conference on Fracture (ECF)*, 30; 2014. p. 1748–53.
- [27] Krupp U, Knobbe H, Christ HJ, Köster P, Fritzen CP. The significance of microstructural barriers during fatigue of a duplex steel in the high- and very-high-cycle-fatigue (HCF/VHCF) regime. *Int J Fatigue* 2010;32(6):914–20.
- [28] Chai G. The formation of subsurface non-defect fatigue crack origins. *Int J Fatigue* 2006;28(11):1533–9.
- [29] Nyström M, Karlsson B. Fatigue of duplex stainless steel influence of discontinuous, spinodally decomposed ferrite. *Mater Sci Eng A* 1996;215(1–2):26–38.
- [30] Akdut N. Phase morphology and fatigue lives of nitrogen alloyed duplex stainless steels. *Int J Fatigue* 1999;21:97–103.
- [31] Marrow TJ, King JE. Microstructural and environmental effects on fatigue crack propagation in duplex stainless steels. *Fatigue Fract Eng Mater Struct* 1994;17(7):761–71.
- [32] Tremisn AS, Gao Y, Dial LC, Grazzi F, Shinohara T. Investigation of microstructure in additive manufactured Inconel 625 by spatially resolved neutron transmission spectroscopy. *Sci Technol Adv Mater* 2016;17(1):324–36.
- [33] Ramadhan RS, Syed AK, Tremisn AS, Kockelmann W, Dalglish R, Chen B, Parfitt D, Fitzpatrick ME. Mapping residual strain induced by cold working and by laser shock peening using neutron transmission spectroscopy. *Mater Des* 2018;143:56–64.
- [34] Connolly M, Slifka A, Drexler E. In situ neutron transmission bragg edge measurements of strain fields near fatigue cracks grown in air and in hydrogen. *International Hydrogen Conference (IHC 2016): Materials Performance in Hydrogen Environments*, 2017.
- [35] Withers PJ. Fracture mechanics by three-dimensional crack-tip synchrotron X-ray microscopy. *Phil Trans R Soc A* 2015;373(2036):20130157.
- [36] Van Tittelboom K, Snoeck D, Vontobel P, Wittmann FH, De Belie N. Use of neutron radiography and tomography to visualize the autonomous crack sealing efficiency in cementitious materials. *Mater Struct Constr* 2013;46(1–2):105–21.
- [37] Iwase K, Sakuma K, Kamiyama T, Kiyanagi Y. Bragg-edge transmission imaging of strain and microstructure using a pulsed neutron source. *Nucl Instrum Methods Phys Res Sect A Accel Spectromet Detect Assoc Equip* 2009;605(1–2):1–4.
- [38] Fermi E, Strum J, Sachs R. The transmission of slow neutrons through microcrystalline. *Phys Rev* 1947;71(9):589–94.
- [39] Kockelmann W, Frei G, Lehmann EH, Vontobel P, Santisteban JR. Energy-selective neutron transmission imaging at a pulsed source, vol. 578; 2007. p. 421–34.
- [40] Santisteban JR, Edwards L, Steuwer A, Withers PJ. Time-of-flight neutron transmission diffraction. *J Appl Crystallogr* 2001;34(3):289–97.
- [41] Woracek R, Penumadu D, Kardjilov N, Hilger A, Strobl M, Wimpory RC, Manke I, Banhart J. Neutron Bragg-edge-imaging for strain mapping under in situ tensile loading. *J Appl Phys* 2011;109(9):1–5.
- [42] Vontobel P, Lehmann EH, Hassanein R, Frei G. Neutron tomography: method and applications. *Phys B Condens Matter* 2006;385-386(1):475–80.
- [43] Sivia DS. *Elementary scattering theory: for X-ray and neutron users*. New York: Oxford University Press; 2011.
- [44] Natterer F, Wübbeling F. *Mathematical methods in image reconstruction*, 5. Siyam; 2001.
- [45] Burca G, Kockelmann W, James JA, Fitzpatrick ME. Modelling of an imaging beamline at the ISIS pulsed neutron source. *J Instrum* 2013;8(10):P10001.
- [46] Chantler CT. Detailed tabulation of atomic form factors, photoelectric absorption and scattering cross section, and mass attenuation coefficients in the vicinity of absorption edges in the soft X-Ray (Z=30–36, Z=60–89, E=0.1 keV–10 keV), addressing convergence issues. *J Phys Chem Ref Data* 2000;29(4):597.
- [47] Drakopoulos M, Connolley T, Reinhard C, Atwood R, Magdysyuk O, Vo N, Hart M, Connor L, Humphreys B, Howell G, Davies S, Hill T, Wilkin G, Pedersen U, Foster A, De Maio N, Basham M, Yuan F, Wanelik K. I12: the joint engineering, environment and processing (JEEP) beamline at diamond light source. *J Synchrotron Radiat* 2015;22(2015):828–38.
- [48] Minniti T, Watanabe K, Burca G, Pooley DE, Kockelmann W. Characterization of the new neutron imaging and materials science facility IMAT. *Nucl Instrum Methods Phys Res Sect A Accel Spectromet Detect Assoc Equip* 2018;888:184–95.
- [49] Lehmann EH, Frei G, Kühne G, Boillat P. The micro-setup for neutron imaging: a major step forward to improve the spatial resolution. *Nucl Instrum Methods Phys Res Sect A Accel Spectromet Detect Assoc Equip* 2007;576(2–3):389–96.

- [50] Griesche A, Dabah E, Kannengiesser T, Kardjilov N, Hilger A, Manke I. Three-dimensional imaging of hydrogen blister in iron with neutron tomography. *Acta Mater* 2014;78:14–22.
- [51] Chen YS, Haley D, Gerstl SSA, London AJ, Sweeney F, Wepf RA, Rainforth WM, Bagot PAJ, Moody MP. Direct observation of individual hydrogen atoms at trapping sites in a ferritic steel. *Science* (80-.). 2017;355(6330):1196–9.
- [52] "Duplex stainless steel plate alloy 2205, Sandmeyer Steel Company." [Online]. Available: <https://www.sandmeyersteel.com/2205.html>.
- [53] Abbey B, Zhang SY, Vorster WJJ, Korsunsky AM. Feasibility study of neutron strain tomography. *Procedia Eng* 2009;1(1):185–8.
- [54] Abbey B, Zhang SY, Vorster W, Korsunsky AM. Reconstruction of axisymmetric strain distributions via neutron strain tomography. *Nucl Instrum Methods Phys Res Sect B Beam Interact Mater Atoms* 2012;270(1):28–35.
- [55] Taylor D. The theory of critical distances. *Eng Fract Mech* 2008;75(7):1696–705.
- [56] Lindley TC, Richards CE, Ritchie RO. The mechanics and mechanisms of fatigue crack growth in metals (a review). *Metall Met Form* 1976;43(9):268–80.
- [57] Si E. Stress intensity factor for surface cracks emanating from the circumferential notch root in notched round bars. *Eng Fract Mech*. 1990;37(4):813–16.
- [58] Minniti T, Kockelmann W, Burca G, Kelleher JF, Kabra S, Zhang SY, Pooley DE, Schooneveld EM, Mutamba Q, Sykora J, Rhodes NJ, Pouzols FM, Nightingale JB, Aliotta F, Bonaccorsi LM, Ponterio R, Salvato G, Trusso S, Vasi C, et al. Materials analysis opportunities on the new neutron imaging facility IMAT@ISIS. *J Instrum* 2016;11(3).
- [59] Tremsin AS, Vallergera JV, McPhate JB, Siegmund OHW, Raffanti R. High resolution photon counting with MCP-timepix quad parallel readout operating at >1 KHz frame rates. *IEEE Trans Nucl Sci* 2013;60(2):578–85.
- [60] Tremsin AS, McPhate JB, Vallergera JV, Siegmund OHW, Feller WB, Lehmann E, Dawson M. Improved efficiency of high resolution thermal and cold neutron imaging. *Nucl Instrum Methods Phys Res Sect A Accel Spectrom Detect Assoc Equip* 2011;628(1):415–18.
- [61] Tremsin AS, Feller WB, Downing RG. Efficiency optimization of microchannel plate (MCP) neutron imaging detectors. I. Square channels with 10B doping. *Nucl Instrum Methods Phys Res Sect A Accel Spectrom Detect Assoc Equip* 2005;539(1–2):278–311.
- [62] Tremsin AS, McPhate JB, Kockelmann WA, Vallergera JV, Siegmund OHW, Feller WB. Energy-resolving neutron transmission radiography at the ISIS pulsed spallation source with a high-resolution neutron counting detector. *IEEE Trans Nucl Sci* 2009;56(5):2931–7.
- [63] Reid A, Martinez I, Marshall M, Minniti T, Kabra S, Kockelmann W, Connolly T, Mostafavi M. Mapping of axial plastic zone for roller bearing overloads using neutron transmission imaging. *Mater Des* 2018;156:103–12.
- [64] Treimer W. Neutron Tomography. Neutron Imaging and Applications Neutron Scattering Applications and Techniques. Bilheux H, McGreevy R, Anderson I, editors. Boston, MA; 2009.
- [65] Kak C, Slaney M. Principles of computerized tomographic imaging. IEEE Press; 1988.
- [66] Miceli D, Minniti T, Formoso V, Kockelmann W, Gorini G. A comparative study of reconstruction methods applied to Neutron Tomography. *J Instrum* 2018;13(6).
- [67] Marone F, Stapanoni M. Re gridding reconstruction algorithm for real-time tomographic imaging. *J Synchrotron Radiat* 2012;19(6):1029–37.
- [68] DSS. ABAQUS analysis user's manual 6.14-2. DSS (Dassault Systèmes Simulia Corp); 2014.
- [69] Roy SC. Modeling and analysis of material behavior during cavitation erosion. *Mater Univ Grenoble Alpes* 2015.
- [70] Woo W, Em V, Seong BS, Shin E, Mikula P, Joo J, Kang MH. Effect of wavelength-dependent attenuation on neutron diffraction stress measurements at depth in steels. *J Appl Crystallogr* 2011;44(4):747–54.
- [71] Kim Y, Kim YM, Koh JY, Lee TH, Woo WC, Han HN. Evaluation of single crystal elastic constants and stacking fault energy in high-nitrogen duplex stainless steel by in-situ neutron diffraction. *Scr Mater* 2016;119:1–4.
- [72] Jia N, Lin Peng R, Brown DW, Clausen B, Wang YD. Tensile deformation behavior of duplex stainless steel studied by in-situ time-of-flight neutron diffraction. *Metall Mater Trans A Phys Metall Mater Sci* 2008;39(13):3134–40.
- [73] Badji R, Bacroix B, Bouabdallah M. Texture, microstructure and anisotropic properties in annealed 2205 duplex stainless steel welds. *Mater Charact* 2011;62(9):833–43.
- [74] Holden TM, Tomé CN, Holt RA. Experimental and theoretical studies of the superposition of intergranular and macroscopic strains in Ni-based industrial alloys. *Metall Mater Trans A* 1998;29(12):2967–73.
- [75] Welvaert M, Rosseel Y. On the definition of signal-to-noise ratio and contrast-to-noise ratio for fMRI data. *PLoS One* 2013;8(11).
- [76] FEI Visualization Sciences Group; 2016.
- [77] Knyazeva M, Pohl M. Duplex steels. Part II: carbides and nitrides. *Metallogr Microstruct Anal* 2013;2:343–51.
- [78] Toda H, Takijiri A, Azuma M, Yabu S, Hayashi K, Seo D, Kobayashi M, Hirayama K, Takeuchi A, Uesugi K. Damage micromechanisms in dual-phase steel investigated with combined phase- and absorption-contrast tomography. *Acta Mater* 2017;126:401–12.
- [79] Mostafavi M, Baimpas N, Tarleton E, Atwood RC, McDonald SA, Korsunsky AM, Marrow TJ. Three-dimensional crack observation, quantification and simulation in a quasi-brittle material. *Acta Mater* 2013;61(16):6276–89.